AGU PUBLICATIONS

JGR

Journal of Geophysical Research: Oceans

RESEARCH ARTICLE

10.1002/2015JC010788

Key Points:
- Observed large tidal modulations to the wavefield on the inner shelf
- SWAN+Delft3D-FLOW model simulates observations accurately
- Model shows modulations are owing to wave-current interaction not depth changes

Correspondence to:
J. Hopkins,
hychenj@mit.edu

Citation:
Hopkins, J., S. Elgar, and B. Raubenheimer (2016), Observations and model simulations of wave-current interaction on the inner shelf, *J. Geophys. Res. Oceans*, *121*, 198–208, doi:10.1002/2015JC010788.

Received 17 FEB 2015
Accepted 4 DEC 2015
Accepted article online 13 DEC 2015
Published online 10 JAN 2016

Observations and model simulations of wave-current interaction on the inner shelf

Julia Hopkins[1], Steve Elgar[2], and Britt Raubenheimer[2]

[1]MIT-WHOI Joint Program in Civil and Environmental Engineering, Cambridge, Massachusetts, USA, [2]Woods Hole Oceanographic Institution, Woods Hole, Massachusetts, USA

Abstract Wave directions and mean currents observed for two 1 month long periods in 7 and 2 m water depths along 11 km of the southern shoreline of Martha's Vineyard, MA, have strong tidal modulations. Wave directions are modulated by as much as 70° over a tidal cycle. The magnitude of the tidal modulations in the wavefield decreases alongshore to the west, consistent with the observed decrease in tidal currents from 2.1 to 0.2 m/s along the shoreline. A numerical model (SWAN and Deflt3D-FLOW) simulating waves and currents reproduces the observations accurately. Model simulations with and without wave-current interaction and tidal depth changes demonstrate that the observed tidal modulations of the wavefield primarily are caused by wave-current interaction and not by tidal changes to water depths over the nearby complex shoals.

1. Introduction

Understanding wave propagation across the continental shelf to the shore is critical to predicting forces on shoreline structures, increases in wave-driven water levels, wave overtopping and flooding, dangerous wave-driven surfzone currents, sediment transport, and beach erosion and accretion. As waves propagate (shoal) over increasingly shallow bathymetry, conservation of energy flux causes wave heights to become larger before breaking. Breaking waves dissipate energy while transferring momentum flux to the water column. In the surf zone, the time-averaged wave-driven forcing raises water levels near the shoreline [*Longuet-Higgins and Stewart*, 1964], producing alongshore varying sea levels and currents [*Apotsos et al*., 2008; *Shi et al*., 2011; *Hansen et al*., 2015] and, in the case of obliquely incident waves, driving alongshore currents in the direction of wave propagation [*Longuet-Higgins*, 1970; *Thornton and Guza*, 1986; *Guza et al*., 1986; *Feddersen et al*., 1998; and many others]. The wave-orbital velocities and wave-generated currents can transport sediment and act as a mechanism for shoreline evolution [*Fredsoe and Deigaard*, 1992; *van Rijn*, 1993; *Amoudry and Souza*, 2011; references therein; and many others].

The energy and direction of waves propagating across the continental shelf to the shore are affected by the bathymetry and by currents, both of which cause shoaling and refraction. Wave energy can be increased by shoaling and decreased by dissipative processes, including bottom friction, whitecapping, and depth-limited breaking. Depth-induced refraction increases with decreasing wave frequency and redirects wave crests to align with bathymetry in shallow water (potentially resulting in areas with wave focusing and shadowing), although breaking waves are not necessarily normally incident. Similarly, currents change wave height and direction by altering the wave number k, given by the linear dispersion relationship:

$$\sigma = \sqrt{gk\tanh(kh)} \tag{1}$$

where σ is the intrinsic wave frequency, g is the gravitational acceleration, and h is the water depth. A current $\boldsymbol{U}$ interacting with the wavefield causes the intrinsic frequency to be Doppler shifted such that the apparent (e.g., observed) frequency ω becomes [*Longuet-Higgins and Stewart*, 1961; *Wolf and Prandle*, 1999]:

$$\omega = \sigma + \boldsymbol{k} \cdot \boldsymbol{U} \tag{2}$$

which, by reapplication of (1) to the Doppler-shifted frequency ω in place of σ, gives a new wave number. Changes in wave number cause changes to energy flux, EC_g, where E is energy and $C_g = F(\omega, k)$ is the group velocity. Changes in wave number likewise affect wave direction, θ. Similar to depth-induced changes,

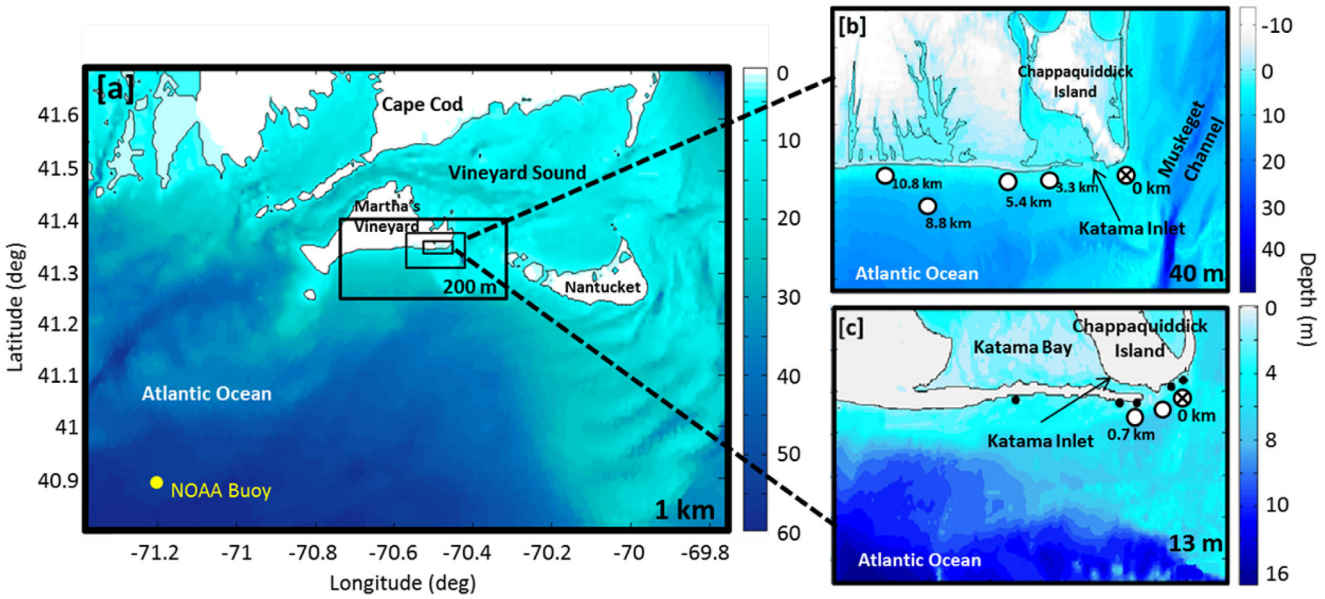

Figure 1. Bathymetry (color contours, scales on the right) and nested grids (black rectangular outlines) for (a) the full model domain, (b) the region near the shoreline of Martha's Vineyard, and (c) the inner grid near the shoreline. Open (7 m depth) and filled (2 m depth) circles are locations of colocated wave and current sensors. The 7 m depth sensors are labeled with their distance (km) from the eastern-most sensor located at $x = 0$ km (open circle with "X"). The sensor at $x = 8.8$ km was in 12 m depth. The yellow circle in Figure 1a is NOAA buoy 44097 (~50 m depth). Spatial resolutions (1000, 200, 40, and 13 m) are shown in the lower right-hand corner of each grid. The sensors in Figure 1b were deployed in 2013, and the sensors in Figure 1c were deployed in 2014. Bathymetric contours near the shoreline of the two inner-most grids are shown in Figure 6.

current-induced changes in θ (relative to the current direction) between two locations (A and B) are given by Snell's Law:

$$k_A \sin(\theta_A) = k_B \sin(\theta_B) \tag{3}$$

There have been many investigations of current-induced wave height growth or decay, usually for the case of currents flowing in the same or opposite direction of the waves [*Gonzalez*, 1984; *Jonsson*, 1990; *Wolf and Prandle*, 1999; *Olabarrieta et al.*, 2011, 2014; *Elias et al.*, 2012; and many others]. There are fewer observational studies of the current-induced changes in wave direction, partially because waves propagating into an opposing or following current ($\theta = 0°$ or 180°), such as commonly occurs near strong jets from inlets, river mouths, and estuaries, do not change direction (equation (3)). The change in direction is maximum for angles near $\theta = 45°$, and increases with current speed and wave frequency (equations (1–3)) [*Wolf and Prandle*, 1999].

Tidal modulations of $\pm 10°$ have been observed in 12–18 m water depth for relatively high-frequency (0.5 Hz) waves [*Wolf and Prandle*, 1999] and in 11 m depth for swell-dominated (0.05–0.30 Hz) wavefields [*Hansen et al.*, 2013]. It was hypothesized that the modulation of the high-frequency wave direction was owing to tidal currents [*Wolf and Prandle*, 1999], and numerical simulations of one tidal cycle suggest the directional changes in the observed swell wavefield likewise were owing to currents, not to tidal changes in water depth [*Hansen et al.*, 2013]. Here tidally modulated changes to wave heights and directions in 7 and 2 m water depths along an Atlantic Ocean shoreline are investigated with both observations from two 1 month long periods and numerical model simulations.

2. Methods

2.1. Field Observations

Water levels, waves, and currents were measured for approximately 1 month along 11 km of the southern shoreline of Martha's Vineyard, MA, (Figure 1) in both August 2013 and July–August 2014. In 2013 and 2014, along the 7 m depth isobath, 1 min mean current profiles in 0.5 m high vertical bins between 0.5 m above the seafloor and the sea surface were obtained with Nortek 1 MHz AWAC acoustic Doppler current profilers for 12 min every half hour, followed by 1024 s of 2 Hz samples of bottom pressure, sea-surface elevation

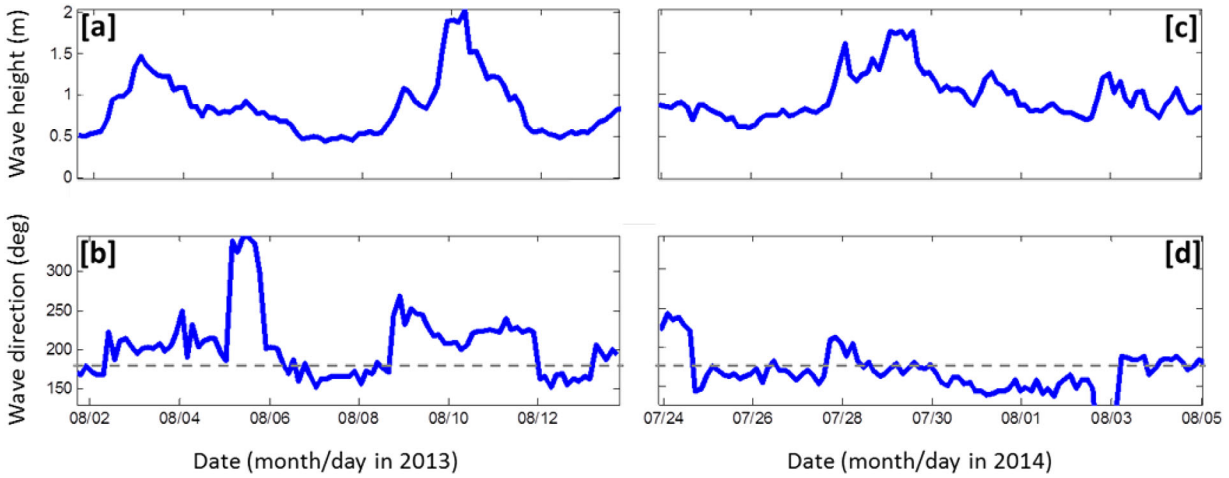

Figure 2. Offshore (a and c) significant wave height and (b and d) wave direction (in nautical coordinates, so that waves coming from the south have direction = 180°) estimated with measurements from the NOAA Waverider buoy in 50 m water depth (Figure 1) in (a and b) 2013 and (c and d) 2014 versus time. The dashed lines at 180° are approximately shore normal in 7 m water depth.

(from a 1 MHz vertical acoustic beam), and near-surface velocities to estimate wave characteristics. In 2013, an additional sensor was deployed in 12 m depth (Figure 1b), 8.8 km west of the eastern-most sensor located at $x = 0$ km. In 2014, 2 Hz observations of currents (0.8 m above the seafloor) and near-bottom pressure were measured with 10 MHz Sontek Triton acoustic Doppler velocimeters at five locations along the 2 m depth isobath from $x = 0$ to $x = 3.3$ km (Figure 1c).

There was little vertical structure to the mean currents in 7 and 12 m depth except in the bottom and top 0.5 m high bins, so the interior bins were used to estimate depth-averaged flows. The two 12 min profiling periods every hour were combined to provide estimates of 1 h means of the depth-averaged currents. One hour averages of the alongshore component of the single-point velocity measurements in 2 m depth are assumed to be representative of depth-averaged alongshore flows. The 2 Hz time series were used to estimate significant wave heights (H_{sig}, 4 times the standard deviation of sea-surface fluctuations) and wave directions [*Kuik et al*., 1988] in the frequency (f) band $0.05 < f < 0.30$ Hz. Bottom pressures were converted to sea-surface elevation using linear wave theory.

The bathymetry in the region is complex (Figure 1), including islands, shoals, and the rapidly migrating Katama Inlet [*Ogden*, 1974] that separates Katama Bay from the Atlantic Ocean. Bathymetric surveys of the shoreline, inlet channel, and ebb shoal near Katama Inlet were performed in summer 2013 and 2014 with a GPS and an acoustic altimeter mounted on a jetski. The horizontal resolution of the jetski surveys is on the order of 10 m, with finer resolution near steep features. Additional bathymetry was obtained during 1998 and 2008 USGS surveys (Northeast Atlantic 3 arc second map, *National Geophysical Data Center* [1999] and Nantucket 1/3 arc second map, *Eakins et al*. [2009]), and has horizontal resolution of 10–90 m. The southern shoreline of Martha's Vineyard is oriented east-west (Figure 1). West of Katama Inlet, bathymetry contours, especially in depths less than ~10 m are roughly parallel to the shoreline (Figure 1b). However, south and east of Katama Inlet and Bay, the bathymetry is cross-shore and alongshore inhomogeneous.

Offshore waves were measured in approximately 50 m depth with a Waverider buoy (Figure 1a, NOAA buoy 44097). Offshore waves were small to moderate ($H_{sig} < 2$ m), usually coming from the south, southwest, or southeast (Figure 2). Tidal currents were more than 2 m/s at the eastern-most 7 m depth sensor ($x = 0$ km, Figure 1), and decreased to less than 0.2 m/s 11 km to the west ($x = 10.8$ km, Figure 1b) (discussed below). Maximum tidal currents in 2 m depth also decreased from east (0.8 m/s at $x \sim 0$ km, Figure 1c) to west (0.2 m/s at $x \sim 3.3$ km, Figure 1b). These observations are consistent with prior studies of tidal propagation in the region [*Chen et al*., 2011], including the phase difference between the 0.5 m amplitude tides in Vineyard Sound and the Atlantic Ocean, which drive tidal currents greater than 2 m/s through Muskeget Channel (Figure 1). To the west of Muskeget Channel, tidal currents weaken and become east-west oriented [*Chen et al*., 2011]. The measured (and modeled) alongshore changes in the tidal modulation of currents, wave heights, and directions (discussed below) in 2 and 7 m water depths in 2014 are consistent with those

in 7 m depth in 2013, suggesting that the westward decrease in tidal modulation is owing to a temporally constant spatial structure, not a change in behavior from 2013 to 2014.

2.2. Numerical Model

A coupled wave and flow numerical model was used to investigate the processes leading to the spatial and temporal structure of the waves and currents observed south of Martha's Vineyard. Waves were modeled with SWAN [*Booij et al*., 1999] by solving the wave action conservation equation, and currents were modeled with Delft3D-FLOW [*Lesser et al*., 2004] by solving the nonlinear shallow water equations. The wave model includes depth-induced and current-induced refraction, and dissipation owing to whitecapping, depth-induced breaking, and bottom friction. Wind was not implemented because observed winds usually were less than 5 m/s (mean (standard deviation) were 2.8 (1.6) and 3.4 (2.0) m/s in 2013 and 2014, respectively). For the conditions observed here, model results with wind were not significantly different than results without wind. Quartet and triad nonlinear interactions were turned off owing to the lack of wind forcing, the relatively short propagation distances in deep water, and the focus on observations seaward of the region of strong quadratic nonlinearities (where $kh \ll 1$). Although quadratic nonlinear interactions are important to many aspects of wave evolution in shallow water [*Freilich and Guza*, 1984], their effects on bulk (energy weighted) statistics of the wavefield (e.g., wave height, average direction, centroidal frequency) are relatively small [*Gorrell et al*., 2011]. The circulation model includes the effects of waves on currents through wave radiation-stress gradients, combined wave and current bed shear stress, and Stokes drift. The wave and flow models were coupled, such that FLOW passes water levels and Eulerian depth-averaged velocities to SWAN, and SWAN passes wave parameters to FLOW, which is run continuously for $\leq$0.25 s time intervals. Similar combined wave and circulation models have been used to investigate wave-current interactions on the inner shelf (8–15 m depth) [*Hansen et al*., 2013], in the surf zone [*Hansen et al*., 2014, 2015; *Chen et al*., 2015], near river mouths [*Elias et al*., 2012], and in coastal bays [*Mulligan et al*., 2010].

SWAN and Delft3D-FLOW (in depth-averaged mode) were run over 3 (2013) and 4 (2014) nested grids (Figure 1a) with both two-way (FLOW) and one-way nesting (SWAN). The outermost grid, with 1 km resolution, spans about 150 km along the north and south boundaries and 100 km along the east and west boundaries. Nested in this coarse grid are finer grids of 200 and 40 m resolution in 2013, and a third grid with 13 m resolution in 2014 to compare with the closely spaced observations ($0 \leq x \leq 0.7$ km, Figure 1c) obtained in 2014. Nesting allows calculations on the coarser grids to serve as boundary conditions for the finer grids, enhancing the resolution of the model near the shoreline with minimal computational cost. The combined USGS large-scale and either the 2013 or the 2014 high-resolution shoreline bathymetry were interpolated onto each of the nested grids.

SWAN has skill in a range of environments, including the inner shelf south of Martha's Vineyard (12–27 m depth) [*Ganju and Sherwood*, 2010; *Ganju et al*., 2011] and many shallow water areas [*Magne et al*., 2007; *Mulligan et al*., 2010], whether forced with observations [*Gorrell et al*., 2011; *Chen et al*., 2015; *Hansen et al*., 2013, 2014, 2015] or with output from global wave models [*van der Westhuysen*, 2010; *Kumar et al*., 2012]. Here, SWAN was run in stationary mode, with wavefield boundary conditions supplied every 3 h. Stationary mode solves for equilibrium wave conditions for a given set of boundary conditions and is less computationally expensive than nonstationary mode. For the 3 h periods and for the wind and wave conditions used here, the assumption of stationarity is not violated even for the largest grid. For the 2013 bathymetry, boundary conditions were a JONSWAP frequency-directional ($\cos^N(\theta)$, where the default value of $N = 20$ was used) spectrum based on the mean wave direction θ, H_{sig}, and average wave period provided by the model WaveWatchIII (WWIII) [*Tolman*, 2002] every 3 km along the open (water) boundaries of the outer grid. The wave model also was run using the frequency-directional spectrum estimated with observations at the buoy in 50 m water depth (Figure 1a) applied uniformly at each point on the boundaries of the outer grid. For southerly waves (which are the most common), model skill was similar for the spatially variable WWIII wave forcing and the spatially uniform buoy forcing. However, model skill was significantly higher with the spatially varying WWIII boundary conditions than with the spatially constant buoy conditions when waves at the buoy came from the north or northeast, in which case the spatially varying wavefield is not represented well by the measurements near the southwest corner of the domain (Figure 1a). WWIII simulations were not available in 2014, so buoy observations were used on the boundaries (wave conditions were southerly). In all cases, SWAN solves the spectral action balance using 36 directional bins (10°/bin) and 37 frequency bands logarithmically spaced between 0.03 and 1.00 Hz. The wave model used a depth-limited

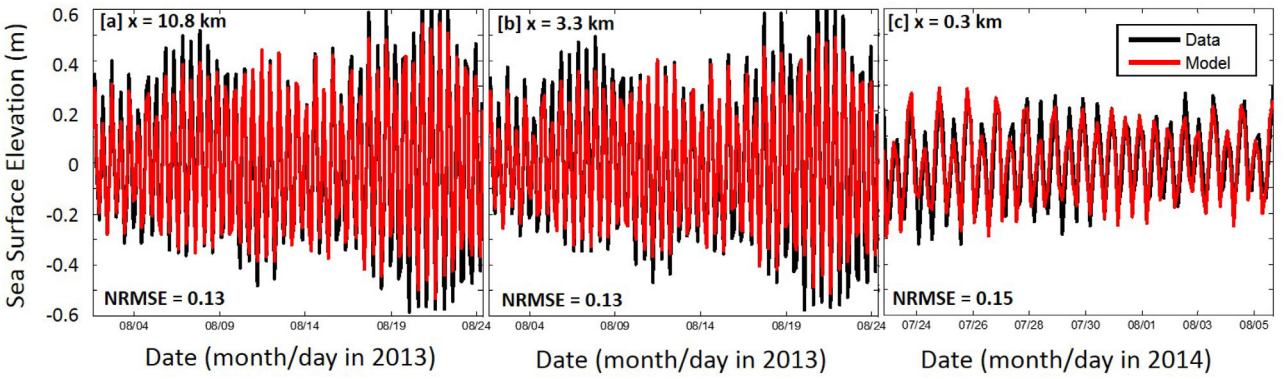

Figure 3. Observed (black curves) and modeled (red curves) 3 h average sea-surface elevations (relative to mean sea level) versus time at locations (Figure 1b) x = (a) 10.8, (b) 3.3, and (c) 0.3 km (distances are relative to the sensor at x = 0 km). RMSE values (normalized by the data range) are given in the lower left-hand corners.

wave breaking formulation without rollers [*Battjes and Janssen*, 1978] with the default value $\gamma = H_{sig}/h = 0.73$, and a JONSWAP bottom friction coefficient associated with wave-orbital motions set higher (0.100 m^2/s^3) than the default (0.067 m^2/s^3) [*Hasselmann et al.*, 1973]. The higher coefficient resulted in more accurate modeled wave heights. Using default coefficients, observed wave heights were under predicted using some friction formulations [*Madsen et al.*, 1988] and over predicted using other approaches [*Collins*, 1972]. Model wave directions were insensitive to the friction formulation.

The circulation model Deflt3D-FLOW solves the time-varying nonlinear shallow water equations on a staggered Arakawa-C grid using an alternating-direction-implicit solver [*Lesser et al.*, 2004] to compute currents throughout the modal domain. The model was run using the 13 most energetic satellite-generated tidal constituents [*Egbert and Erofeeva*, 2002] along open boundaries, which were dominated by the M2 (~80% of the variance, with small changes depending on location along the boundary) and N2 (~10% of the variance) constituents. In addition, the model used a free slip condition at closed (land) side boundaries, a spatially uniform Chezy roughness of 65 $m^{0.5}/s$ (roughly equivalent to a drag coefficient of $C_d = 0.0023$) at bottom boundaries, and default Delft3D parameters for coupling the FLOW and WAVE models [*Deltares*, 2014]. Second-order differences were used with a time step of 0.25 s for 2013 (40 m spacing in the highest resolution grid) and 0.15 s for 2014 (13 m spacing) for numerical stability.

Model parameters (e.g., time steps, grid resolution) were chosen to accommodate future studies of shoreline evolution in the Katama region on time scales varying from that of individual storms to seasons to years. Spatial and temporal resolutions are fine enough for numerical stability and verification with observations. Using higher resolution does not change simulation results significantly and requires more computational effort.

3. Results

Model predictions of the sea levels, waves, and currents are comparable with observations in 7 and 2 m water depths in the area south of Martha's Vineyard. The model simulates the observed 3 h sea level fluctuations (primarily the M2 tide) fairly well (within a few cm), although occasionally it underpredicts the minima and maxima by as much as 0.10–0.15 m (Figure 3). These model-data differences could be owing to imperfect tidal boundary conditions, inaccurate model bathymetry, or unmodeled physical processes. Similar to previous results [*van der Westhuysen*, 2010; *Mulligan et al.*, 2010; *Gorrell et al.*, 2011; *Hansen et al.*, 2015; and many others], the model skillfully predicts the wave heights observed in 7 (Figures 4a–4c) and 2 m (Figures 5a and 5b) depth. Model-data wave height discrepancies in shallow water (e.g., Figure 5b) could be caused by inaccurate model bottom friction, incorrect model simulations of sea level, or inaccurate model bathymetry. The small errors in wave height (which typically are over estimated at all tide levels) are more likely owing to inaccurate bathymetry than to the under estimation of the range of sea level fluctuations. The model also skillfully predicts the wave directions (Figures 4d–4f and 5c, 5d), including the large tidal modulations observed near the eastern edge of the domain (x = 0.3 km, Figure 4f).

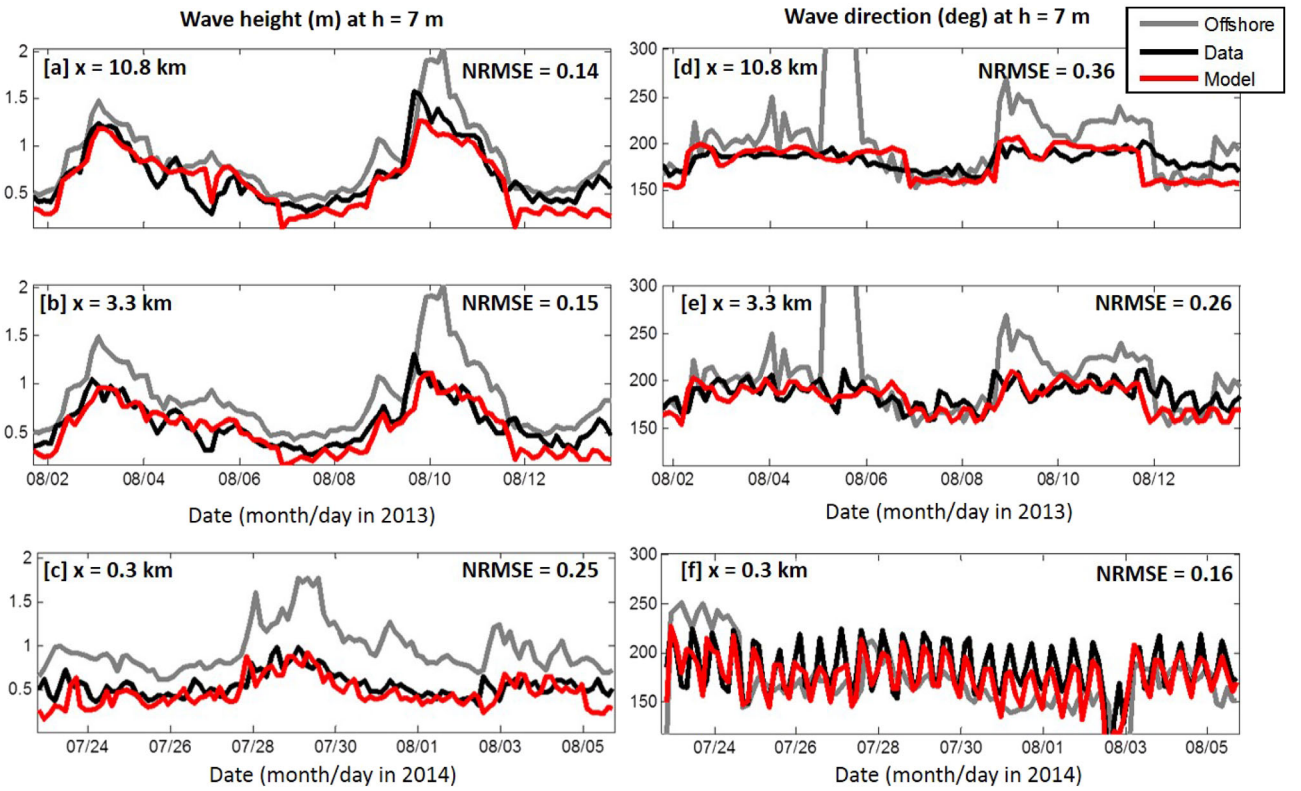

Figure 4. Observed (black curves) and modeled (red curves) 3 h (a–c) significant wave height and (d–f) wave direction in 7 m water depth versus time at locations (Figure 1) x = (a and d) 10.8, (b and e) 3.3, and (c and f) 0.3 km (distances are relative to the sensor at x = 0 km). Gray curves are the observed offshore (50 m depth) wave heights and directions. RMSE values (normalized by the data range) are given in the upper right-hand corners.

Model simulations suggest strong spatial inhomogeneity in wave heights (Figure 6a) and directions (Figure 6b) onshore of the complex bathymetry, similar to nearshore waves in other locations [*Apotsos et al.*, 2008; *Hansen et al.*, 2013; *Chen et al.*, 2015; and others] and consistent with the observations (colored circles in Figure 6). The tidal modulation of wave heights (Figures 4 and 5) varied along the shoreline, resulting in a tidally varying alongshore change in wave height (e.g., Figure 6a) in 7 m depth from 0 to as much as 35% of the offshore wave height (Figure 7). The model simulates both the magnitude (Figure 6a) and the tidal modulation (Figure 7b) of the observed alongshore gradient in wave height fairly well.

Likewise, the amplitude of the observed mean currents (primarily M2) decreases from east (Figures 8c and 8f, black curves) to west (Figures 8b, 8e and 8a, 8d, black curves) by an order of magnitude, and is modeled well (Figure 8, red curves). At the eastern edge of the domain (x = 0.3 km), near the strong tidal flows in Muskeget Channel (Figure 1), the model underestimates the western component of the flow (Figure 8c), possibly owing to incorrect modeling of flow separation near the southeast corner of Chappaquiddick Island (Figure 1). Model simulations (not shown) suggest that the size and location of the region of flow separation are sensitive to bathymetry, which may not be accurate near the separation region. Model skill is higher a few km to the west (e.g., x = 3.3 km, Figure 8b), away from the separation region. Model-data discrepancies in the relatively small cross-shore (north-south) flows (Figures 8d–8f) may be owing to neglect of cross-shore winds, Stokes-Coriolis currents [*Lentz et al.*, 2008], and three-dimensional effects, or to incorrect bathymetry in the model.

The relatively strong tidal flows and the tidal changes in water depth can result in refraction and tidal modulation of the wavefield (including heights and directions), especially at the eastern edge of the domain where currents are strongest (Figures 8c and 8f) and the offshore bathymetry is most inhomogeneous (Figures 1 and 6). For example, the amplitudes of the M2 component of the observed and modeled tidal currents and wave directions are largest in the east (x = 0 km) and decrease to the west (x = 10.8 km)

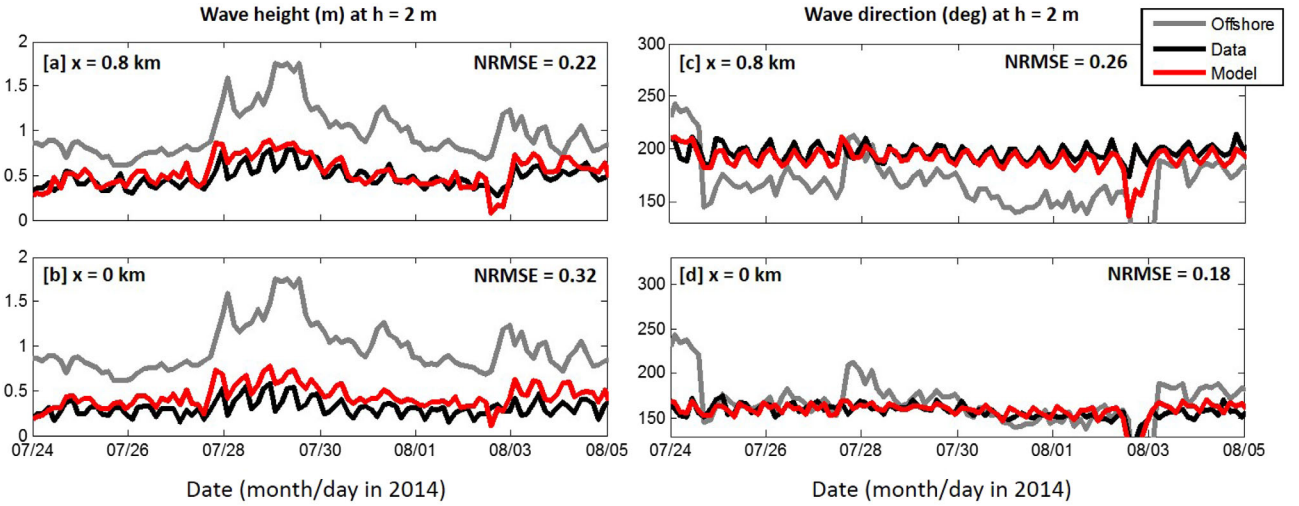

Figure 5. Observed (black curves) and modeled (red curves) 3 h (a and b) significant wave height and (c and d) wave direction in 2 m water depth versus time at locations (Figure 1) x = (a and c) 0.8 and (b and d) 0 km (distances are relative to the sensor at x = 0 km). Gray curves are the observed offshore (50 m depth) wave heights and directions. RMSE values (normalized by the data range) are given in the upper right-hand corners.

(Figure 9). Near the eastern edge of the domain ($x < 0.5$ km, Figure 9), the model under predicts the M2 amplitudes of the mean currents (Figures 8c and 9) and the wave directions, possibly because horizontal flow separation around Chappaquiddick Island becomes important in this region. Additionally, small errors in the amplitude of tidal boundary conditions could contribute to mismatch between simulated and observed current and wave direction M2 amplitudes.

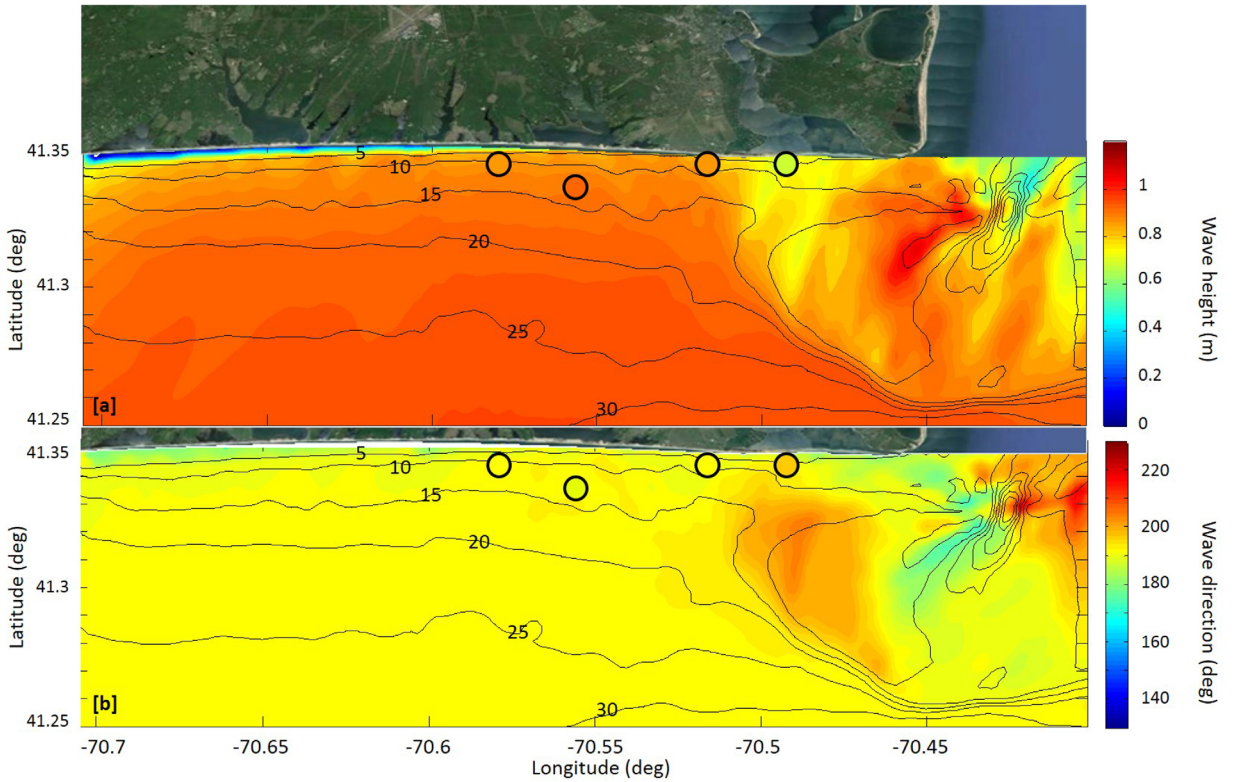

Figure 6. Spatial distribution (color contours, scales on the right) of modeled (a) significant wave height and (b) wave direction on 3 August 2013 09:00 h EDT during flood tide (flow from west to east into Muskeget Channel). Black curves are depth contours every 5 m, and the black circles are filled with the color of the observed values at those locations. If model and data agree, the color inside the circle matches the color of the surrounding model contours.

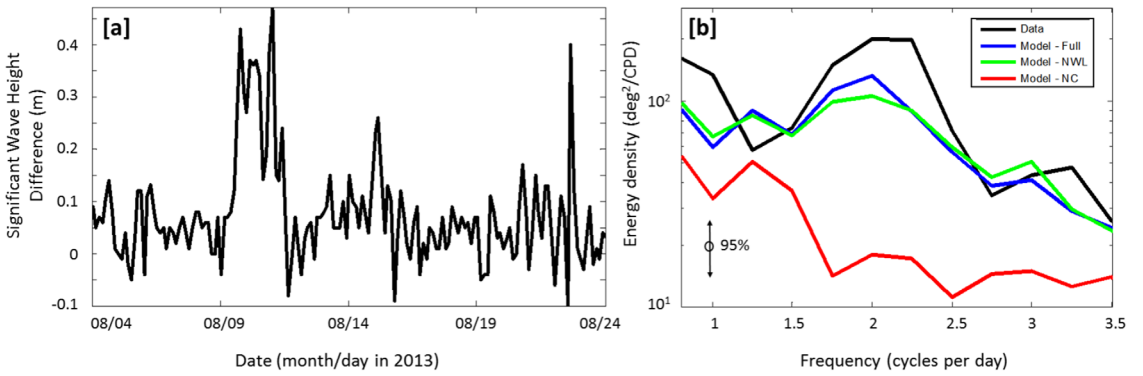

Figure 7. (a) Difference between the significant wave height observed in 7 m depth at $x = 3.3$ km and at $x = 10.8$ km versus time. (b) Energy density of the time series of alongshore difference in wave height versus frequency for observations (black curve) and simulated by the model including tidal currents and water depth changes (blue curve), currents, but no depth changes (green curve), and depth changes, but no currents (red curve). The spectra have 36 degrees of freedom, and the 95% confidence levels are shown.

To determine if the M2 fluctuations in the wavefield are caused by depth-induced or current-induced refraction or both, the model was run with both currents and tidal depth oscillations, with tidal depth oscillations, but no currents, and with currents, but no tidal depth oscillations. The observed tidal fluctuations in the alongshore gradient of wave heights are simulated better by the model with currents and depth changes (compare the blue with the black curve in Figure 7b) than by the model with depth changes only (Figure 7b, red curve). The modeled gradients with currents, but no depth changes (Figure 7b, green curve) are similar to those using the full model (currents and depth changes, Figure 7b, blue curve), suggesting the modulations of the alongshore gradients in wave heights primarily are caused by current-induced refraction.

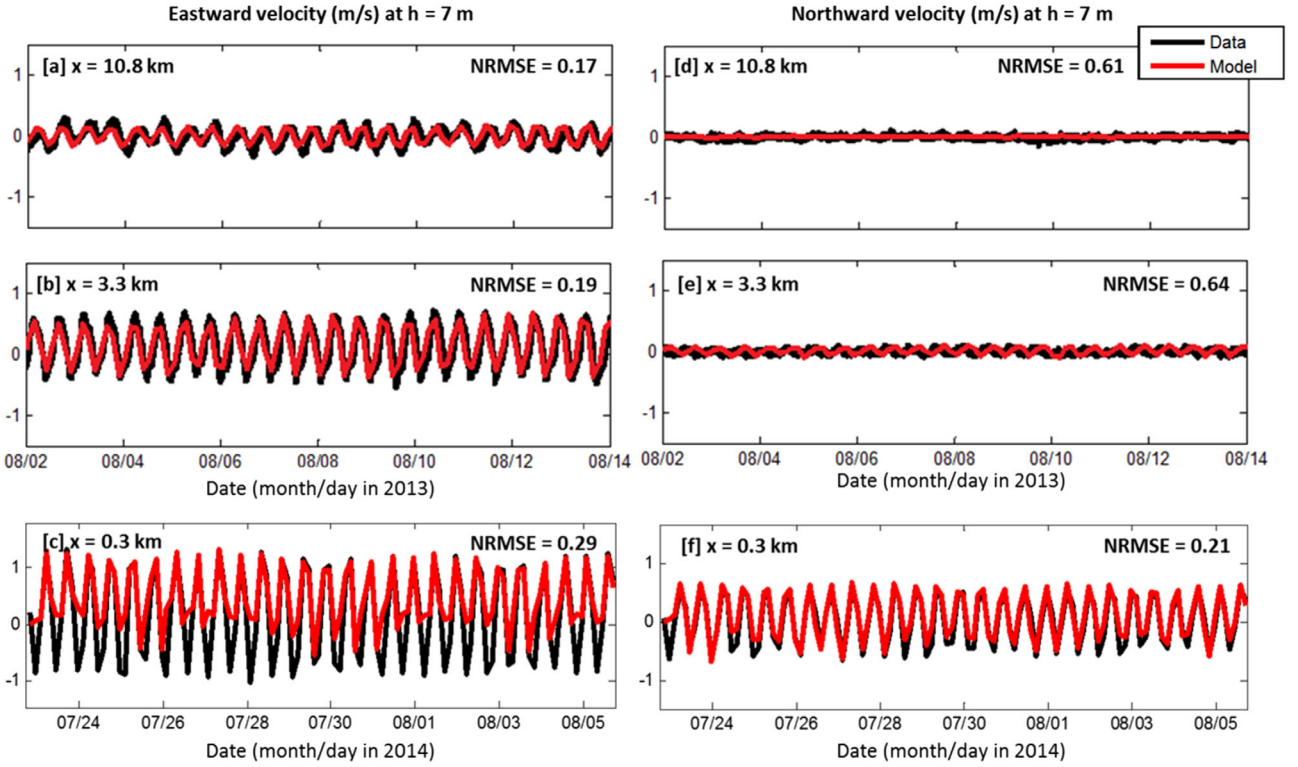

Figure 8. Observed (black curves) and modeled (red curves) 1 h mean depth-averaged (a–c) east and (d–f) north velocity in 7 m water depth versus time at locations (Figure 1) $x =$ (a and b) 10.8, (c and d) 3.3, and (e and f) 0.3 km. RMSE values (normalized by the data range) are given in the upper right-hand corners.

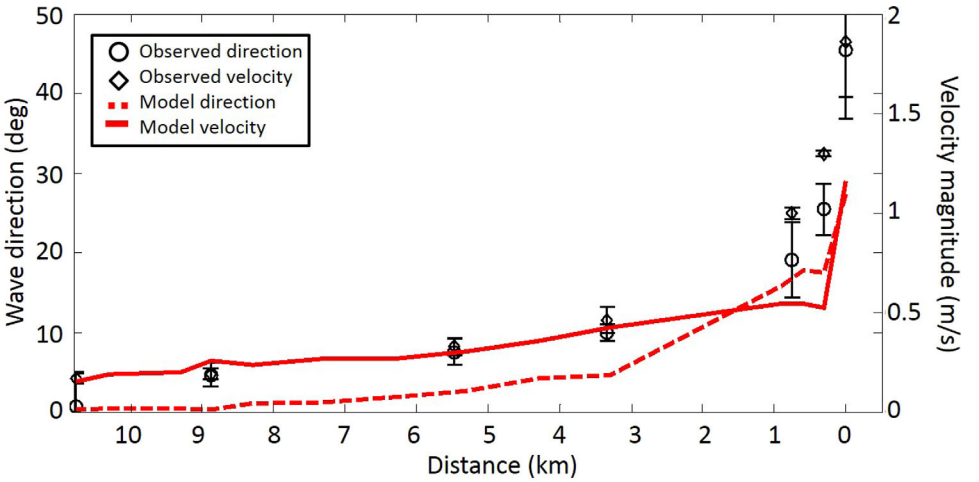

Figure 9. Amplitude of the observed (black symbols) and modeled (red curves) tidal (M2) modulation of wave direction (open circles, dashed curve) and velocity magnitude (open diamonds, solid curve) in 7 m depth versus distance from the eastern-most sensor ($x = 0$ km, Figure 1). 95% confidence intervals of the M2 amplitude estimates, calculated using a tidal frequency analysis of the time series ("T_TIDE") [*Pawlowicz et al.*, 2002] are shown for the observations. Some of the error bars for the observed velocity magnitude are smaller than the diamond symbols. The errors in estimating model amplitudes (not shown) are similar to those from the observations.

Model tests and equations (1–3) suggest that the observed tidal modulation in wave direction also is owing to currents and not depth changes. For 0.1 Hz waves propagating from 50 to 7 m depth across tidally varying currents with similar magnitudes to observed flows in Muskeget Channel, equations (1–3) predict large (±∼35°) modulations to the wave direction, comparable with the observations (Figures 4e, 4f, 5c, 5d, and 9) and with the model simulations that account for a frequency-directional spectrum and spatially varying currents and bathymetry (Figure 10, blue curves). In contrast, the observed tidal modulations of wave direction are not reproduced by the model when currents are not included (Figure 10, red curves), but are reproduced for the model with currents, but no tidal depth changes (Figure 10, green curves). Similar to previous model runs for one tidal cycle [*Hansen et al.*, 2013], the simulations suggest that the observed tidal modulations of wave direction are caused primarily by current-induced refraction. As waves refract over the bathymetry between 7 and 2 m depth, the tidal modulation of direction is reduced to about ±10° relative to shore-normal (Figures 5c and 5d). Consequently, alongshore currents (and associated sediment flux) driven by breaking waves may change direction (or strengthen and weaken) with the tide, even when offshore wave conditions are constant.

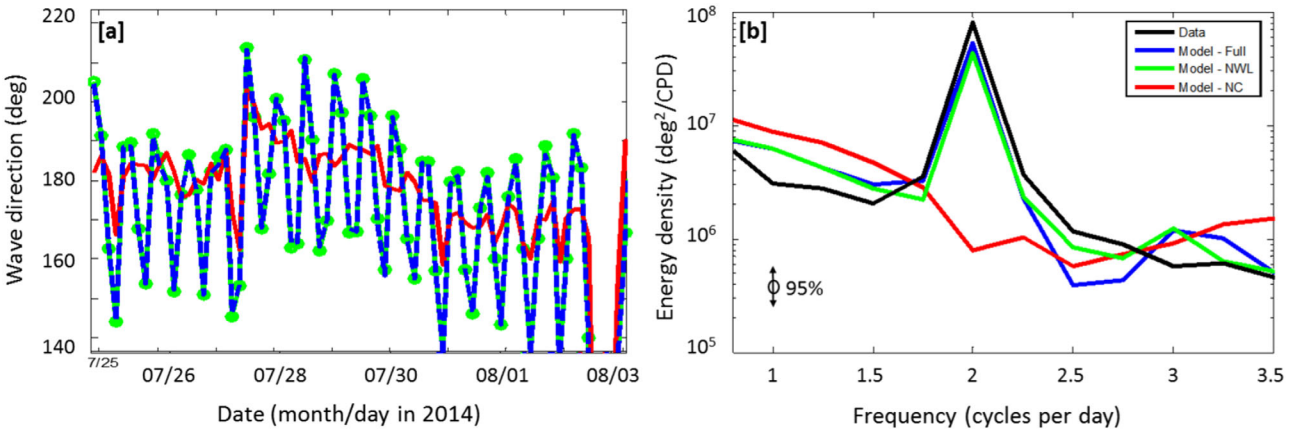

Figure 10. (a) Wave direction versus time at $x = 0.3$ km and (b) energy density of the time series of wave direction versus frequency for observations (Figure 10b only, black curve) and simulated by the model including tidal currents and water depth changes (blue curves), currents, but no depth changes (green curves), and depth changes, but no tidal currents (red curves). The spectra have 36 degrees of freedom, and the 95% confidence levels are shown. Model-data time series comparisons are given in Figure 4f.

4. Conclusions

A combined wave (SWAN) and circulation (Delft3D-FLOW) numerical model accurately simulates waves and currents observed in 7 and 2 m water depths near Katama Bay and Inlet, on the southern shoreline of Martha's Vineyard, MA in the presence of strong (>2 m/s) tidal currents and complex bathymetry. The model reproduces the alongshore gradients in waves and mean currents, as well as the large (±35°) tidal modulation of wave directions observed for two 1 month long periods. Model simulations with and without wave-current interactions demonstrate that the modulations of the wavefield primarily are owing to current-induced refraction, and not to tidal changes in water levels. The comparisons with observations suggest that the model with wave-current interaction and with the parameters used here simulates waves and currents accurately in regions with complex bathymetry and strong currents. These results further suggest that tidal modulations in wave direction in other coastal environments with complex bathymetry and strong currents also could be owing to wave-current interaction.

Acknowledgments

The data used in this study are available by contacting the authors, hychenj@mit.edu or elgar@whoi.edu. Support was provided by ONR, NSF, Sea Grant, NDSEG, an MIT Presidential Graduate Fellowship, and ASD(R&E). Mumen Alzubi, Kohl Brinkman, Danik Forsman, Janet Fredericks, Levi Gorrell, Liliana Montoya, Mara Orescanin, Maddie Smith, Anna Wargula, and Billy Wells helped obtain the observations, and Jeff Hansen provided valuable help with modeling.

References

Amoudry, L. O., and A. J. Souza (2011), Deterministic coastal morphological and sediment transport modeling: A review and discussion, *Rev. Geophys.*, *49*, RG2002, doi:10.1029/2010RG000341.

Apotsos, A., B. Raubenheimer, S. Elgar, and R. T. Guza (2008), Wave-driven setup and alongshore flows observed onshore of a submarine canyon, *J. Geophys. Res.*, *113*, C07025, doi:10.1029/2007JC004514.

Battjes, J. A., and J. P. M. Janssen (1978), Energy loss and set-up due to breaking of random waves, in Proceedings of the 16th International Conference on Coastal Engineering, 569 pp., ASCE, N. Y.

Booij, N., R. C. Ris, and L. H. Holthuijsen (1999), A third-generation wave model for coastal regions: 1. Model description and validation, *J. Geophys. Res.*, *104*(C4), 7649–7666, doi:10.1029/98JC02622.

Chen, C., H. Huang, R. C. Beardsley, Q. Xu, R. Limeburner, G. W. Cowles, and H. Lin (2011), Tidal dynamics in the Gulf of Maine and New England Shelf: An application of FVCOM, *J. Geophys. Res.*, *116*, C12010, doi:10.1029/2011JC007054.

Chen, J.-L., T. J. Hsu, F. Shi, B. Raubenheimer, and S. Elgar (2015), Hydrodynamics and sediment transport modeling of New River Inlet (NC) under the interaction of tides and waves, *J. Geophys. Res. Oceans*, *120*, 4028–4047, doi:10.1002/2014JC010425.

Collins, J. I. (1972), Prediction of shallow-water spectra, *J. Geophys. Res.*, *77*(15), 2693–2707, doi:10.1029/JC077i015p02693.

Deltares, (2014), *Delft3D-Wave: Simulation of Short Crested Waves With SWAN, User Manual*, Deltares, Delft, Netherlands.

Eakins, B. W., L. A. Taylor, K. S. Carignan, R. R. Warnken, E. Lim, and P. R. Medley (2009). Digital elevation model of Nantucket, Massachusetts: Procedures, data sources and analysis, *NOAA Tech. Memo. NESDIS NGDC-26*, 29 pp., Dep. of Commerce, Boulder, Colo.

Egbert, G. D., and S. Y. Erofeeva (2002), Efficient inverse modeling of barotropic ocean tides, *J. Atmos. Oceanic Technol.*, *19*, 183–204.

Elias, E. P. L., G. Gelfenbaum, and A. J. Van der Westhuysen (2012), Validation of a coupled wave-flow model in a high-energy setting: The mouth of the Columbia River, *J. Geophys. Res.*, *117*, C09011, doi:10.1029/2012JC008105.

Feddersen, F., R. T. Guza, S. Elgar, and T. H. C. Herbers (1998), Alongshore momentum balances in the nearshore, *J. Geophys. Res.*, *103*(C8), 15,667–15,676, doi:10.1029/98JC01270.

Fredsoe, J., and R. Deigaard (1992), *Mechanics of Coastal Sediment Transport*, World Sci. Publ., Singapore.

Freilich, M. H., and R. T. Guza (1984), Nonlinear effects on shoaling surface gravity waves, *Philos. Trans. R. Soc. London Ser. A*, *311*, 1–41.

Ganju, N. K., and C. R. Sherwood (2010), Effect of roughness formulation on the performance of a coupled wave, hydrodynamic, and sediment transport model, *Ocean Modell.*, *33*(3–4), 299–313, doi:10.1016/j.ocemod.2010.03.003.

Ganju, N. K., S. J. Lentz, A. R. Kirincich, and J. T. Farrar (2011), Complex mean circulation over the inner shelf south of Martha's Vineyard revealed by observations and a high-resolution model, *J. Geophys. Res.*, *116*, C10036, doi:10.1029/2011JC007035.

Gonzalez, F. I. (1984), A case study of wave-current-bathymetry interactions at the Columbia River Entrance, *J. Phys. Oceanogr.*, *14*, 1065–1078.

Gorrell, L., B. Raubenheimer, S. Elgar, and R. T. Guza (2011), SWAN predictions of waves observed in shallow water onshore of complex bathymetry, *Coastal Eng.*, *58*(6), 510–516, doi:10.1016/j.coastaleng.2011.01.013.

Guza, R. T., E. B. Thornton, and N. Christensen Jr. (1986), Observations of steady longshore currents in the surf zone, *J. Phys. Oceanogr.*, *16*, 1959–1969.

Hansen, J. E., E. Elias, J. H. List, L. H. Erikson, and P. L. Barnard (2013), Tidally influenced alongshore circulation at an inlet-adjacent shoreline. *Cont. Shelf Res.*, *56*, 26–38, doi:10.1016/j.csr.2013.01.017.

Hansen, J. E., T. T. Janssen, B. Raubenheimer, F. Shi, P. L. Barnard, and I. S. Jones (2014), Observations of surfzone alongshore pressure gradients onshore of an ebb-tidal delta, *Coastal Eng.*, *91*, 251–260, doi:10.1016/j.coastaleng.2014.05.010.

Hansen, J., B. Raubenheimer, J. List, and S. Elgar (2015), Modeled alongshore circulation and force balances onshore of a submarine canyon, *J. Geophys. Res. Oceans*, *120*, 1887–1903, doi:10.1002/2014JC010555.

Hasselmann, K., et al. (1973), Measurements of Wind-Wave Growth and Swell Decay During the Joint North Sea Wave Project (JONSWAP), *Dtsch. Hydrogr. Z. Suppl.*, *8*(12), 1–95.

Jonsson, I. G. (1990), Wave–current interactions, in *Ocean Engineering Science: The Sea*, vol. 9A, edited by B. Le Méhauté and D. M. Hanes, pp. 65–120, Harvard Univ. Press, Cambridge, Mass.

Kuik, A. J., G. P. van Vledder, and L. H. Holthuijsen (1988), A method for the routine analysis of pitch-and-roll buoy wave data, *J. Phys. Oceanogr.*, *18*, 1020–1034.

Kumar, N., G. Voulgaris, J. C. Warner, and M. Olabarrieta (2012), Implementation of the vortex force formalism in the coupled ocean-atmosphere-wave-sediment transport (COAWST) modeling system for inner shelf and surf zone applications, *Ocean Modell.*, *47*, 65–95, doi:10.1016/j.ocemod.2012.01.003.

Lentz, S., M. Fewings, P. Howd, J. Fredericks, and K. Hathaway (2008), Observations and a model of undertow over the inner continental shelf, *J. Phys. Oceanogr.*, *38*(11), 2341–2357, doi:10.1175/2008JPO3986.1.

Lesser, G. R., J. A. Roelvink, J. A. T. M. van Kester, and G. S. Stelling (2004), Development and validation of a three-dimensional morphological model, *Coastal Eng.*, *51*, 883–915, doi:10.1016/j.coastaleng.2004.07.014.

Longuet-Higgins, M. S. (1970), Longshore currents generated by obliquely incident sea waves: 1, *J. Geophys. Res.*, *75*(33), 6778–6789, doi:10.1029/JC075i033p06778.

Longuet-Higgins, M. S., and R. W. Stewart (1961), The changes in amplitude of short gravity waves on steady non-uniform currents, *J. Fluid Mech.*, *10*(4), 529–549, doi:10.1017/S0022112061000342.

Longuet-Higgins, M. S., and R. W. Stewart (1964), Radiation stresses in water waves; a physical discussion, with applications, *Deep Sea Res. Oceanogr. Abstr.*, *11*(4), 529–562, doi:10.1016/0011-7471(64)90001-4.

Madsen, O., Y.-K. Poon, and H. Graber (1988), Spectral wave attenuation by bottom friction: Theory, in *Proceedings 21th International Conference Coastal Engineering*, pp. 492–504, ASCE, Hamburg, Germany.

Magne, R., K. Belibassakis, F. Herbers, T. Ardhuin, W. O'Reilly, and V. Rey (2007), Evolution of surface gravity waves over a submarine canyon, *J. Geophys. Res. 112*, C01002, doi:10.1029/2005JC003035.

Mulligan, R. P., A. E. Hay, and A. J. Bowen (2010), A wave-driven jet over a rocky shoal, *J. Geophys. Res.*, *115*, C10038, doi:10.1029/2009JC006027.

National Geophysical Data Center (1999), *U.S. Coastal Relief Model—Northeast Atlantic*, Natl. Oceanic and Atmos. Admin., Boulder, Colo., doi:10.7289/V5MS3QNZ.

Ogden, G. (1974), Shoreline changes along the southeastern coast of Martha's Vineyard, Massachusetts for the past 200 years, *Quat. Res.*, *4*, 496–508.

Olabarrieta, M., J. C. Warner, and N. Kumar (2011), Wave-current interaction in Willapa Bay, *J. Geophys. Res.*, *116*, C12014, doi:10.1029/2011JC007387.

Olabarrieta, M., W. R. Geyer, and N. Kumar (2014), The role of morphology and wave-current interaction at tidal inlets: An idealized modeling analysis, *J. Geophys. Res. Oceans*, *119*, doi:10.1002/2014JC010191.

Pawlowicz, R., B. Beardsley, and S. Lentz (2002), Classical tidal harmonic analysis including error estimates in MATLAB using T_TIDE, *Comput. Geosci.*, *28*, 929–937.

Shi, F., D. M. Hanes, J. T. Kirby, L. Erikson, P. Barnard, and J. Eshleman (2011), Pressure-gradient-driven nearshore circulation on a beach influenced by a large inlet-tidal shoal system, *J. Geophys. Res.*, *116*, C04020, doi:10.1029/2010JC006788.

Thornton, E. B., and R. T. Guza (1986), Surf zone longshore currents and random waves: Field data and models, *J. Phys. Oceanogr.*, *16*, 1165–1178.

Tolman, H. L. (2002), User manual and system documentation of WAVEWATCH-III version 2.22, *Tech. Rep*. *222*, Natl. Weather Serv./Natl. Cent. for Environ. Predict./Mar. Model. and Anal. Branch, NOAA, Silver Spring, Md.

van der Westhuysen, A. J. (2010). Modeling of depth-induced wave breaking under finite depth wave growth conditions, *J. Geophys. Res.*, *115*, C01008, doi:10.1029/2009JC005433.

van Rijn, L. (1993), *Principles of Sediment Transport in Rivers, Estuaries and Coastal Seas*, Blokzijl, Aqua Publ., Netherlands.

Wolf, J., and D. Prandle (1999), Some observations of wave–current interaction, *Coastal Eng.*, *37*(3–4), 471–485, doi:10.1016/S0378-3839(99)00039-3.